Rationalizing the influence of the Mn(IV)/Mn(III) red-Ox transition on the electrocatalytic activity of manganese oxides in the oxygen reduction reaction

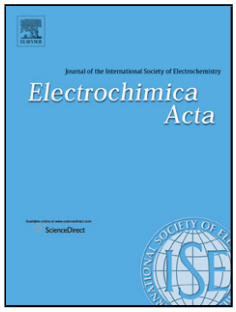

Title: Rationalizing the Influence of the Mn(IV)/Mn(III) Red-Ox Transition on the Electrocatalytic Activity of Manganese Oxides in the Oxygen Reduction Reaction

Author: Anna S. Ryabova Filipp S. Napolskiy Tiphaine Poux Sergey Ya. Istomin Antoine Bonnefont Denis Antipin Alexander Ye. Baranchikov Eduard E. Levin Artem M. Abakumov Gwénaëlle Kéranguéven Evgeny V. Antipov Galina A. Tsirlina Elena R. Savinova

PII: S0013-4686(15)30784-2
DOI: http://dx.doi.org/doi:10.1016/j.electacta.2015.11.012
Reference: EA 26012

To appear in: *Electrochimica Acta*

Received date: 23-8-2015
Revised date: 3-11-2015
Accepted date: 3-11-2015

Please cite this article as: Anna S.Ryabova, Filipp S.Napolskiy, Tiphaine Poux, Sergey Ya.Istomin, Antoine Bonnefont, Denis Antipin, Alexander Ye.Baranchikov, Eduard E.Levin, Artem M.Abakumov, Gwénaëlle Kéranguéven, Evgeny V.Antipov, Galina A.Tsirlina, Elena R.Savinova, Rationalizing the Influence of the Mn(IV)/Mn(III) Red-Ox Transition on the Electrocatalytic Activity of Manganese Oxides in the Oxygen Reduction Reaction, Electrochimica Acta http://dx.doi.org/10.1016/j.electacta.2015.11.012

Rationalizing the Influence of the Mn(IV)/Mn(III) Red-Ox Transition on the Electrocatalytic Activity of Manganese Oxides in the Oxygen Reduction Reaction

Anna S. Ryabova[a,b], Filipp S. Napolskiy[a], Tiphaine Poux [b,1], Sergey Ya. Istomin[a], Antoine Bonnefont[c], Denis Antipin[a], Alexander Ye. Baranchikov[d], Eduard E. Levin[a], Artem M. Abakumov[e], Gwénaëlle Kéranguéven[b], Evgeny V. Antipov[a], Galina A. Tsirlina[a], Elena R. Savinova[b,2]

[a]Moscow State University, Leninskie Gory, 1-str. 3, Moscow 119991, Russia

[b] ICPEES, UMR 7515 CNRS-ECPM-Université de Strasbourg, 25, rue Becquerel, F 67087 Strasbourg Cedex 2, France

[c] IC, UMR 7177, CNRS- Université de Strasbourg, 4 rue Blaise Pascal, 67000 Strasbourg, France

[d]Kurnakov Institute of General and Inorganic Chemistry RAS, 31 Leninsky prospect, Moscow 119991, Russia

[e]EMAT, University of Antwerp, Department of Physics, Groenenborgerlaan 171, B-2020 Antwerp, Belgium

[1] Present address :
Paul Scherrer Institut, CH-5232 Villigen PSI, Switzerland
[1] Corresponding Author:

elena.savinova@unistra.fr

Abstract

Knowledge on the mechanisms of oxygen reduction reaction (ORR) and descriptors linking the catalytic activity to the structural and electronic properties of transition metal oxides enable rational design of more efficient catalysts. In this work ORR electrocatalysis was studied on a set of single and complex Mn(III) oxides with a rotating disc electrode method and cyclic voltammetry. We discovered an exponential increase of the specific electrocatalytic activity with the potential of the surface Mn(IV)/Mn(III) red-ox couple, suggesting the latter as a new descriptor for the ORR electrocatalysis. The observed dependence is rationalized using a simple mean-field kinetic model considering availability of the Mn(III) centers and adsorbate-adsorbate interactions. We demonstrate an unprecedented activity of Mn_2O_3, ca. 40 times exceeding that of MnOOH and correlate the catalytic activity of Mn oxides to their crystal structure.

Keywords: manganese oxides; oxygen reduction reaction (ORR); red-ox transition; rotating disc electrode (RDE); meanfield kinetic modeling

1. Introduction

Transition metal oxides (TMOs) have attracted much attention as promising catalysts for the electrochemical oxygen reduction reaction (ORR) in alkaline media in view of their potential applications for metal-air batteries, fuel cells, and, recently, also for regenerative fuel cells [1] [2] [3]. Manganese oxides are of particular interest as low cost, abundant and green materials with high electrocatalytic activities in the ORR and the OER (oxygen evolution reaction) [4]. It is the observation, early in the 19th century, of the sensitivity of MnO_2 cathode of the Leclanché's element to air, which stimulated interest in oxygen electrocatalysis on Mn oxides and lead to the introduction of zinc-air batteries (see Ref. [5] and references therein). Since then, numerous studies have been performed in order to evaluate the activity, understand the ORR mechanism, and unveil structure - activity relationships in ORR electrocatalysis on Mn oxides [6] [7] [8] [9] [10] [11] [12] [13] [14]. Despite the fact that numerous single and complex Mn oxides have been studied as the ORR catalysts, the main structural and compositional factors determining their electrocatalytic activity are still poorly understood, and the values of electrocatalytic activities reported in the literature are often contradictory. This may be attributed to a number of factors, such as electrochemical degradation of Mn oxides at excessively high or low electrode potentials [11], or insufficient electronic conductivities of some Mn oxides, prompting researchers to add carbon to the catalytic layers [6] [14] [15] [16] [17]. Considering that in alkaline media carbon also participates in the ORR [18], singling out the contributions of the oxide and of carbon to the ORR activity is not a trivial task, and the reported activities may change by order(s) of magnitude depending on the presence of carbon and on its amount [17]. A yet another difficulty relates to the fact that there is no common view on which parameter to use to characterize the catalytic performance. For the case of the OER, this is well discussed by Fabbri et al. [19]. Materials are compared in terms of the ORR onset (or potential at a specified current) neglecting the catalyst loading and its specific surface area, or in terms of current at a defined potential (usually 0.9 V vs RHE) normalized to the mass or surface area of the oxide.

These uncertainties complicate understanding of the structure-activity relationships in the ORR electrocatalysis by oxides.

Already early studies attempted to find ORR/OER descriptors which could be further used for guiding the design and optimization of the TMO catalysts. A prediction of the OER activity increase with the M-OH bond strength for metal electrodes [20], raised attempts to correlate the OER activity of perovskite oxides with the enthalpy of formation of corresponding hydroxides [21]. Importance of the red-ox transitions of metal cations has also been recognized [22], supported by a "volcano" relationship of the OER activity *vs.* the enthalpy of lower-to-higher oxide transition for a wide range of oxides [23]. Goodenough and Cushing [24] and Suntivich *et al.* [25] applied molecular orbital considerations and proposed the e_g-orbital occupancy activity descriptor, which postulates that the latter determines the strength of the oxygen bonding to metal oxide surfaces and thus the ORR/OER activity. By studying a range of perovskite-type oxides of various transition metals it was conjectured that an e_g occupancy slightly below 1 is required for achieving high ORR activity [25] [26].

In the last decades application of first-principles computational methods using density functional theory (DFT) offered a molecular level insight into the elementary steps of reactions on surfaces. Su *et al.* [27] performed periodic DFT calculation for Mn oxides, and considered an "associative" mechanism of the ORR and OER occurring through the formation of OH_{ads}, O_{ads} and OOH_{ads} intermediates. By establishing a "scaling relationship" between the adsorption strength of OOH_{ad} and that of OH_{ad}, Su *et al.* suggested Gibbs energy of OH formation (ΔG_{OH}) as a unique ORR descriptor and predicted similar ORR activities for Mn_3O_4, Mn_2O_3 and MnO_2.

Recently, from combined experimental and kinetical modeling studies on the ORR on perovskite-type oxides, we discovered that the measured ORR activity strongly depends on the amount of carbon which had to be introduced in the catalytic layer for improving its electronic conductivity and maximizing the utilization of the catalyst active centres, and worked out the tools to extract the specific activity of oxides [17]. Then, we came to the conclusion that Mn-

perovskites are much better ORR catalysts compared to Co-based counterparts, the latter only acting as co-catalysts in tandem with carbon. Finally, by studying the ORR and the oxidation/reduction reactions of its stable intermediate, hydrogen peroxide, and by combining experimental studies with a mean-field kinetic model, we arrived at the conclusion that the apparent $4e^-$ ORR on (Mn and Co) TMOs with the perovskite structure follows a "series" $2e^-+2e^-$ pathway, where the O_2 molecule is first reduced to hydrogen peroxide, the latter reacting on the catalyst surface to produce water [28] [29]. We put forward a kinetic model, which is based on the reaction mechanism shown in Figure 1. The model is not only capable of reproducing the experimental data on the ORR and H_2O_2 red-ox transformations in a wide range of experimental parameters, but helps predicting factors responsible for the activity of TMOs. The mechanism shown in Figure 1 builds on earlier studies [7] [24] [25] [26] [28] and is based on the assumption of the key role played by the M(n)/M(n+1) red-ox transition (steps 1 and 5 in Figure 1). Note that red-ox transformations of Mn cations in the potential interval of the ORR/OER have been confirmed by *in situ* XAS [10] [30] and *ex situ* XRD studies [31].

Armed with the knowledge acquired recently on the oxygen electrocatalysis on TMOs, in this publication we seek for establishing the structure-activity relationship by studying a set of Mn oxides adopting different crystal structures (Figure 2): Mn_2O_3, MnOOH, $A_{1-x}A'_xMnO_3$ perovskites ($LaMnO_3$, $PrMnO_3$, $La_{0.8}Ca_{0.2}MnO_3$), MnO_2, and Mn_3O_4. All of them (with the exception of MnO_2) primarily contain Mn(III) cations (Mn_3O_4 contains 2/3 Mn(III) and 1/3 Mn(II), and $La_{0.8}Ca_{0.2}MnO_3$ contains 4/5 Mn(III) and 1/5 Mn(IV)), and are expected to satisfy the e_g-occupancy requirement of efficient ORR electrocatalysis proposed in refs [24] [25]. By juxtaposing the ORR activity measured with a rotating disc electrode (RDE) with surface red-ox properties of oxide materials studied with cyclic voltammetry (CV), we arrive at the conclusion that the potential of the surface Mn(IV)/Mn(III) red-ox transition can be used as a descriptor of the ORR activity. We complement this with the mean-field modeling in order to rationalize the observed behavior and to provide a self-consistent phenomenological description of the

interfacial red-ox mediator ORR catalysis. We explore adsorbate coverage effects and a likely influence of lateral adsorbate interactions.

2. Experimental

2.1. Sample preparation

MnOOH sample was prepared according to the procedure described in Ref. [32]. Aqueous solution of $KMnO_4$ was added to a stirred solution, containing sucrose, $MnSO_4$and HNO_3. The resultant mixture was refluxed at 100 °C under constant stirring for 4 h. MnO_2 and Mn_3O_4 were prepared by thermal decomposition of MnOOH for 2h at 240°C (in air) and 600°C (in Ar), respectively (*cf.* thermal gravimetric analysis in Figure S1 of ESI). Three Mn_2O_3 samples were studied in this work. The first one (**Mn_2O_3_wet1**, refer to Table 1 for sample notations) was prepared by aerosol spray pyrolysis [33]. The aerosol was produced from 0.3 M $Mn(CH_3COO)_2$ aqueous solution using ultrasonic generator operated at 2.64 MHz. The obtained aerosol was directed to the furnace by an air flow where pyrolysis occurred at 800-900 °C. The second sample (**Mn_2O_3_wet3**) was obtained by calcination of an amorphous product of co-proportionation of $Mn(CH_3COO)_2$ and $KMnO_4$ in air at 550 °C for 12 h [34]. **Mn_2O_3_wet_2** sample was discarded, since it was not a single phase. Commercially available Mn_2O_3 ("Reachim", Russia) was milled in the planetary-type mill Fritsch Pulveresitte 6 operated at 120 rpm for 30 min in ethanol with the addition of fish oil (**Mn_2O_3_milled**) and used for comparison purposes. $LaMnO_3$, $PrMnO_3$, $La_{0.8}Ca_{0.2}MnO_3$ perovskites were prepared by the procedure described in Ref. [35]. Briefly, La_2O_3, Pr_6O_{11}, and $CaCO_3$ were first reacted with nitric acid to form nitrates, and then mixed with $Mn(CH_3COO)_2$. Then aqueous solutions of precursors were mixed with acrylamide and bis-acrylamide and slowly heated up to 300°C to form a polyacrylamide gel. The gel was annealed in air at 650°C for 1h to produce desired perovskite oxides, which thereafter were milled in a planetary mill for 3 h at 120 rpm using WC balls.

2.2. Sample characterization

Phase composition was determined by X-ray powder diffraction (XRPD) with a Huber G670 Image plate Guinier diffractometer ($CuK_{\alpha 1}$ radiation, curved Ge monochromator, image plate detector), and (for Mn_2O_3 samples) also with a Rigaku D/Max RC powder diffractometer (CuK_{α} radiation, graphite analyser crystal, scintillation counter). The instrumental line profile broadening effects were measured on the NIST SRM 660a (LaB_6) standard. Microstructural analysis (domain size distribution) was performed within the framework of the Whole Powder Pattern Modeling (WPPM) approach using the PM2K software package [36] [37].

Thermogravimetric (TG) analysis was performed in synthetic air (20% O_2, 80% Ar), Ar (g) or O_2 (g) in the temperature range from 25 to 800 °C with a heating rate of 3 °C min^{-1} using Netzsch STA 449C thermoanalyser.

Scanning electron microscopy (SEM) measurements were performed with Carl Zeiss NVision 40 operated at 1-20 kV. High angle annular dark field scanning transmission electron microscopy (HAADF-STEM) images were obtained with an aberration-corrected Titan G3 electron microscope operated at 300 kV.

Specific surface area was determined by N_2 physisorption using ASAP 2010 analyser (Micromeritics, USA) by multiple point Brenauer-Emmett-Teller (BET) approach.

2. 3. Electrode preparation and electrochemical measurements

Oxides were deposited as thin films on a glassy carbon (GC) support. Compared to our previous work [17] the electrode preparation procedure was modified in order to improve the oxide/carbon contact. Namely, a required amount of carbon and oxide was first ground in a mortar, and then a desired sample weight was mixed with ultra-pure water (18.2 M Ωcm, <3 ppb TOC, Purelab) to prepare an ink which was ultrasonicated for 30 min, and drop cast onto the upper face of a GC rod (0.07 cm^2 geometric area) of an Autolab rotating disc electrode (RDE) polished to a mirror finish using alumina paste (down to 0.05 μm). The layer was dried, and then

2 μL of an alkaline ionomer AS-4 from Tokuyama Company (8.68 μL As-4 in 4 mL H_2O) was deposited onto it and again dried under N_2. The oxide/carbon mass ratio was varied until an optimum 1:1 ratio was established The latter allowed decreasing the Ohmic resistance without an excessive increase of the electrode layer thickness (for the influence of carbon on RDE curves of selected samples the reader is referred to Figure S2 of the Electronic Supplementary Information, ESI). If not otherwise stated the loading was 91 $\mu g.cm^{-2}_{geo}$ both for oxide and for carbon. Carbon of the Sibunit family [38] [39] with BET surface area 65.7 $m^2 g^{-1}$ was chosen for its high purity and high electronic conductivity. Pt/C catalyst (40 wt.% Pt on carbon black, Alfa Aesar) was used for benchmarking.

Electrochemical measurements were performed in 1M NaOH electrolyte in a standard three-electrode cell at 25°C using Autolab potentiostat (PGSTAT302N) equipped with an analog scan generator. All parts of the electrochemical cell in contact with the alkaline electrolyte were from Teflon and the remaining parts were from Pyrex glass. The electrolyte was prepared from extra pure NaOH solution (Acros Organics, 50 wt.% aqueous solution) and ultra-pure water (18.2 MΩ cm, < 3 ppb TOC, Purelab). The working electrode was an RDE described above. The counter electrode was a Pt wire and the reference electrode was a Hg/HgO/1 M NaOH electrode (0.93 V vs. Reversible Hydrogen Electrode, RHE). In what follows all potentials (*E*) are referred to the RHE scale. The electrolyte resistance determined from the high frequency part of the electrochemical impedance spectra (measured in the 1 Hz to 100 kHz range) was equal to ca. 15 Ohm.

Cyclic voltammograms (CVs) were obtained in N_2-purged electrolyte at a scan rate of 10 mV s^{-1} within a stability potential window determined for each oxide sample individually. RDE voltammograms were obtained in O_2-saturated electrolyte at rotation rates from 400 till 2500 rpm at a 10 mV s^{-1} scan rate. Under these conditions the difference between the positive and the negative-going scans after the background correction (a CV under N_2 atmosphere) was negligible. RDE currents are normalized to the geometric area of the electrode and corrected to

the background currents measured in the N_2 atmosphere. Only positive RDE scans are shown in the figures. Ohmic drop correction was not applied. Kinetic currents are calculated via mass-transport correction of the RDE voltammograms following a standard procedure described in our previous publication [17] and normalized to the BET surface area of oxides after subtraction of the kinetic ORR current on carbon. For Pt/C, "electrochemical" surface area determined from desorption of "under-potentially deposited hydrogen" was applied.

3. Kinetic modeling

Microkinetic modeling was applied in order to rationalize the influence of the Mn(IV)/Mn(III) red-ox potential and the presence of adsorbate-adsorbate interactions on the ORR activity. Determining the exact values of the rate constants was beyond the scope of this work. The modeling is based on the ORR mechanism proposed in our previous work [28] [29] and shown schematically in Fig. 1 and also presented in the ESI. This model was able to reproduce semi-quantitatively the oxygen reduction and the hydrogen peroxide oxidation/reduction data for Mn and Co based perovskites for various catalyst loadings in a wide range of H_2O_2 concentrations [28]. At variance from our previous work [29], the contribution of carbon to the ORR activity was neglected in order to simplify the model. The O_{ad} and OH_{ad} species were assumed to be coordinated to the Mn(IV) and Mn(III) surface sites, respectively. All electron transfer processes were mathematically modeled assuming Butler-Volmer electrochemical kinetics. Frumkin-type isotherm was used to account for the adsorbate-adsorbate interactions. The ORR current-potential curves were simulated under steady-state conditions assuming a linear concentration profile for O_2 and HO_2^- in the diffusion layer. The kinetic equations as well as the values used for simulations can be found in the ESI.

4. Results

4. 1. Phase composition and microstructure

X-ray Powder Diffraction (XRPD) analysis confirmed formation of highly crystalline target phases (phase compositions are given in Table 1, while XRPD patterns are shown in Figure S3 of the ESI). Morphology of the samples was examined with SEM (Figure 3). The MnOOH, MnO_2 and Mn_3O_4 samples are polydisperse, consisting of a mixture of round and rod-like crystals. Three Mn_2O_3 specimens exhibit different morphologies. The Mn_2O_3_wet1 sample, prepared at 800 – 900 ^oC, shows micron-sized sintered faceted crystals. The Mn_2O_3_milled sample, prepared from commercial specimen by ball milling, contains sintered particles with the size < 100 nm. The Mn_2O_3_wet3 sample, prepared at 550 ^oC, demonstrates the lowest particle size (~ 50 nm) and agglomeration degree. BET surface area (Table 1) in the Mn_2O_3_wet1 - Mn_2O_3_milled - Mn_2O_3_wet3 series increases with decreasing the particle size from 3 to 27 $m^2\ g^{-1}$. All perovskite oxides show similar morphology, consisting of sintered ca. 20 – 40 nm crystals.

4.2. Formal potentials of surface Mn(IV)/Mn(III) red-ox transition

Cyclic voltammetry (CV) with a decreasing negative potential limit was applied to determine the stability window of oxide materials in 1M NaOH and establish characteristic potentials of surface red-ox transitions (Figure 4). Typical CVs acquired in the potential interval from 0.5 to 1.15 V are compared in Figure 5a. Note that for MnO_2 the shape of CVs changes with the negative shift of the cathodic potential limit, suggesting that the surface of the sample degrades at low potentials.

In the potential range from 0.7 to 1.15 V, corresponding to the onset of the ORR (Figure 5b), all materials show red-ox peaks, which may be attributed to the Mn(IV)/Mn(III) transition of surface cations [10] [40]. The reaction scheme shown in Figure 1 suggests that adsorption of O_2 molecule requires availability of a Mn(III) site on the oxide surface. Thus, the Mn(IV)/Mn(III)

red-ox transition, corresponding to the Mn(IV)=O/Mn(III)-OH conversion (step 1 in Figure 1) is an important step, which in what follows is characterized by formal potential (E_f) calculated as a half-sum of the respective anodic and cathodic peak potentials (see Figure S4 of ESI). In the series of investigated Mn oxides E_f spans from 0.88 to 0.99 V, showing the most positive values for the Mn_2O_3 samples (Table 1). In what follows we will show that higher E_f values for Mn_2O_3 compared to MnOOH oxide lead to more than an order of magnitude higher ORR rate for the former.

4.3. ORR on manganese oxide/carbon composites

Figure 4b shows RDE curves acquired in O_2-saturated 1 M NaOH for selected samples at 900 rpm. RDE voltammograms for other materials are presented in the Figure S5 of ESI. One may notice a significant positive shift of the ORR onset potential for Mn_2O_3_wet3 compared to MnOOH, even though the BET surface area of the latter exceeds that of Mn_2O_3_wet3 by a factor of 2 (Table 1), and both contain Mn(III), and thus, according to the e_g-occupancy criterion [24] [25], might be expected to have comparable activities. One may also see that the ORR onset for Mn_2O_3_wet3 is similar to that of Pt/C. The effective number of electrons transferred in the ORR was calculated from the slope of Koutecky–Levich plots at 0.65 V vs. RHE (Figure 6) and tabulated in Table 1. For the Mn_2O_3 samples as well as for perovskite oxides n_{eff} is close to 4, while for MnO_2, MnOOH and Mn_3O_4 it is around 3, suggesting that half of O_2 is reduced to water, while half is transformed into H_2O_2. Note however that for a "series" ORR mechanism occurring via an intermediate hydrogen peroxide formation, the release of the latter in the electrolyte, and the ensuing n_{eff} depend on the catalyst loading [29] explaining different n_{eff} values reported in the literature.

One may also notice significant differences between the samples at potentials below 0.75 V, where RDE currents attain their limiting values. According to our recent studies of the H_2O_2 reduction, which will be subject of a forthcoming publication, for MnOOH, MnO_2 and Mn_3O_4

samples, the limitation results from a slow chemical step (step 5 in Figure 1) rather than from slow diffusion.

It is instructive to compare kinetic currents shown in Figure 5c (Tafel plots), which were obtained after mass transport correction of the RDE curves and normalization to the BET surface area of oxide materials. Tafel plots demonstrate the highest specific (surface weighted) activity for Mn_2O_3 samples, and the lowest for the MnO_2 and MnOOH samples among all studied materials. The span in the specific activities of Mn oxides (40-fold at 0.9 V vs RHE) is significantly larger than the difference of surface density of Mn cations at their surfaces (Table S1 of the ESI). Note that at high potentials (0.90 – 0.95 V vs. RHE) the specific activity of Mn_2O_3 is only by factor of 4 inferior of that of Pt. It is worth mentioning that while the ORR onset for the three investigated Mn_2O_3 samples is very different (see Figure S5a of ESI) and, as expected, shifts positive following the increase of their BET surface areas from Mn_2O_3_wet1 (3 $m^2\ g^{-1}$) to Mn_2O_3_milled (8 $m^2\ g^{-1}$) and then to Mn_2O_3_wet3 (27 $m^2\ g^{-1}$), their specific activities are essentially the same in the potential range from 0.85 to 0.95 V. This fact underscores the importance of normalizing kinetic ORR currents to the surface areas determined either by BET (this work), or by other suitable methods [41]. Note that the exceptionally high activity of Mn_2O_3_wet3 sample prevents correct determination of kinetic currents at potentials below 0.85 V, where measured currents are approaching the diffusion-limited value. All Tafel plots in Figure 5c demonstrate bending, which in what follows will be rationalized using the kinetic model.

To verify the dependence of the ORR activity on the Mn(IV)/Mn(III) red-ox transition, in Figure 5d we plot surface-weighted ORR kinetic currents j_k *vs.* E_f. The figure demonstrates that j_k increases exponentially with the positive shift of the formal potential of surface red-ox Mn(IV)/Mn(III) couple, supporting the importance of the latter for the ORR mechanism. Similar red-ox potential effect has been observed in ORR electrocatalysis by metal complexes [42] but to the best of our knowledge has not been documented for transition metal oxides yet. The effect of

degradation is exemplified for MnO_2, which shows a 2-fold ORR activity difference depending on the cathodic potential limit (Figure 5d). Note that cycling to potentials inferior of 0.4 V *vs*. RHE has a negative impact on the ORR activities of all samples. However, such low values are outside the potential interval of interest for fuel cell applications. Detailed investigation of degradation phenomena will be subject of a forthcoming publication.

Comparing mass activity, specific activity and half-wave potentials from this work with the literature data for various Mn oxides (Table 2) reveals an exceptional performance of Mn_2O_3_wet3 in the ORR, which in what follows is attributed to the high formal potential of its surface Mn(IV)/Mn(III) cations. Note also that the mass-weighted ORR activity of Mn_2O_3_wet3 is higher, and the half-wave potential more positive than the values reported for Mn_2O_3 in the literature. This may be explained by (i) the high (27 m^2 g^{-1}) specific surface area of Mn_2O_3_wet3, (ii) the integrity of the bixbyite structure during electrocatalysis thanks to respecting the oxide stability interval, and (iii) our improved preparation procedure of the thin electrode layer and an optimized oxide/carbon ratio (see Experimental), which maximize utilization of the oxide surface.

4.4. Kinetic modeling

Further insights into the dependence of the ORR activity on the red-ox properties of the Mn oxide surface can be gained by comparing the experimental results with the predictions of the kinetic model. Linking the ORR activity with the surface potential of the Mn(IV)/Mn(III) transition requires reconstructing the adsorption isotherm, that is the O_{ad} coverage (θ_O) as a function of the electrode potential *E*. Unfortunately, lack of the information on the potential of zero O_{ad} coverage, as well as likely presence of concurrent processes contributing to the anodic and cathodic charging currents in CVs, prevented us from building realistic adsorption isotherms from the experimental data. To better understand the role of Mn(IV)/Mn(III) couple in the ORR electrocatalysis, CVs and corresponding O_{ad} isotherms were simulated for a set of parameters

and shown in Figure 7a-c. A simplified kinetic model presented in our previous work [28] [29] was based on the Langmuir adsorption isotherm, which assumed an absence of adsorbate-adsorbate interactions. In this work we consider a more realistic Frumkin isotherm and explore the effect of the interaction parameter γ, which was varied from 0 (no adsorbate-adsorbate interactions, Langmuir-type isotherm) to 10 (strong O_{ad} – O_{ad} repulsion), and the standard surface red-ox potential $E°_1$ of the Mn(IV)/Mn(III) couple. Simulated CVs in Figure 7a,b show that an increase of $E°_1$ at fixed γ shifts the red-ox peaks and the corresponding θ_O vs. E isotherms simulated for stationary conditions (Figure 7c) toward more positive potentials without modification of their shape. Note that the experimentally determined E_f is related to the standard potential $E°_1$ as follows: $E_f = E_1^\circ + \frac{RT\gamma}{2F}$. That is, for γ=0 E_f is equal to $E_1°$, and E_f linearly increases with $E_1°$ for constant γ. On the other hand, the increase of γ from 0 to 10 at a constant value of $E°_1$ leads to a significant broadening as well as a positive shift of the anodic and cathodic peak potentials (*cf.* Figure 7a and b). In this case the O_{ad} isotherms exhibit similar onset potentials, their slope decreasing with the increase of γ. Furthermore, it should be noticed, that the increase of either $E°_1$ or γ induces a lower O_{ad} coverage at a given potential (Figure 7c) and thus a higher fraction of Mn(III) sites available for the O_2 adsorption.

Comparison of experimental (Figure 5a) and simulated (Figure 7a,b) CVs suggests that the former differ from those expected for Langmuir-type adsorption, manifesting a pronounced repulsive interaction between the O_{ad} species at the surface of the metal oxide particles. However, determination of the exact values of γ is hindered by the presence of significant background currents in the experimental CVs.

The RDE ORR curves were simulated for various $E°_1$ and γ values. Other model parameters (Table S2) were kept constant, although their actual values may also vary depending on the oxide crystal structure. The RDE ORR current potential curves are plotted in Figure 7d for the set of $E°_1$ and γ values already considered in Figure 7,b. The onsets as well as the shapes of the simulated ORR current-potential curves are strongly affected by the $E°_1$ and γ values, the

ORR activity always increasing with E_f (Figure 7d) in agreement with the experimental data (Figure 5d). The modification of the shape of the ORR curves can be better seen using the Tafel representation constructed after mass transport correction of the current-potential curves. In good agreement with the experimental data, a change in the Tafel slope from 120mV/decade for E<0.85V to 30-50mV/decade for E >0.95V can be observed in the simulated plots (Figure 7e). The change in the Tafel slope occurring between 0.85 and 0.95V (depending on the sample) is caused by the decrease of the fraction of Mn(III) sites available for O_2 and HO_2^- adsorption when the electrode potential is increased (*cf*. Figure 7c). It should be noticed that at high overpotentials, when the Mn(III) surface coverage is high, the Tafel slope is close to 120mV/decade whatever the value of the Frumkin interaction parameter. In contrast, the Tafel slope at low overpotentials is significantly affected by the repulsive interactions in the O_{ad} layer, the slope increasing from 30 to ca. 50mV/decade when γ is increased from 0 to 6. Note however that the value of the Tafel slope in the low overpotential region depends also on other parameters such as the ratio between the rate constants of steps (2) and (3) in Figure 1, and also on possible lateral interactions between other adsorbed intermediate species of the ORR that are not taken into account in our simulations.

Finally, the correlation between the ORR kinetic current determined at 0.95 V and the red-ox peak position E_f is displayed in Figure 7f for three different cases: (i) increasing $E°_1$ at constant γ=0 (blue), (ii) increasing $E°_1$ at constant γ=6 (green), and (iii) increasing γ at constant $E°_1$ =0.85 V (magenta). In all cases, the ORR kinetic current increases with E_f, in agreement with the experimental data. For γ=0, (case (i)), the model predicts an exponential increase of the ORR activity with a slope of ca. 60 mV/decade up to a potential of 0.95 V in agreement with the experimental finding. The exponential increase of the activity with $E°_1$ is mainly caused by the increase of the number of available active Mn(III) sites in the range of the ORR onset potential. Since similar trends are observed in the experiment and in simulations, it might be concluded that the ORR activity of Mn oxides is limited by the oxidation of the Mn(III) active sites into

Mn(IV), the latter not being capable to adsorb either O_2 or HO_2^- species. For a higher γ=6, (case (ii)) the simulations also yield an increase of the ORR activity with E_f but with a smaller slope than in case (i). For such γ values, strong repulsive interactions between O_{ad} adsorbates prevent total blocking of the catalyst surface by Mn(IV) species for $E°_1$ values below ca. 0.92 V, resulting in higher ORR activities (*cf*. blue and green symbols in Figure 7f). On the other hand, only a limited gain in the number of Mn(III) sites and thus in the ORR activity can be obtained for higher $E°_1$ values. In case (iii), increasing γ at fixed $E°_1$ yields the j_k *vs*. E_f curve with a convex shape, showing that while the presence of weak repulsive interactions between the O_{ad} species is expected to result in a significant improvement of the ORR activity, only a limited improvement of the latter is expected when γ increases above 6. Overall, these results demonstrate that not only the red-ox peak position but also the shape of the CV and the presence of lateral adsorbate-adsorbate interactions should be analyzed for better understanding of the influence of Mn(IV)/Mn(III) red-ox couple on the ORR activity. Comparing model calculations (Fig. 7) with the experimental data (Fig. 5), we can unambiguously indicate E_f as the main factor responsible for the observed difference in the ORR activities of studied Mn oxides. Judging from the shapes of CVs under N_2 atmosphere, one may assume that γ does not differ significantly for the set of studied materials. Finally, it is worth mentioning that in our ORR model, some O_{ad} species are also formed during the HO_{2ad} decomposition (step (5) in Figure 1), suggesting that the rate of HO_2^- reduction will also be affected by the Mn(IV)/Mn(III) red-ox transition.

4.5. Microstructure of Mn_2O_3 catalysts

It is remarkable that the Mn_2O_3 samples demonstrate exceptional specific electrocatalytic activity regardless the synthetic procedure, the ensuing morphology and their specific surface area (spanning from 3 to 27 $m^2\ g^{-1}$). In order to better understand this, the samples Mn_2O_3_wet1 and Mn_2O_3_wet3 with very different morphologies (*cf*. SEM images in Figure 3) were studied with transmission electron microscopy. Figure 8 shows HAADF-STEM images of Mn_2O_3

nanoparticles at low (a, c, e) and high (b, d, f) magnification. In the Mn_2O_3_wet3 sample one can observe separate round-shaped nanoparticles with the size of 20 – 100 nm as well as interconnected curved elongated particles (Figure 8a, c). In Mn_2O_3_wet1 the faceted particles from 50 nm up to few hundred nm in size are highly agglomerated forming framework structures (Figure 8e). This correlates well with the crystallite size distribution in the Mn_2O_3 samples determined from XRPD data using WPPM (Table S3 of ESI). In both samples particles are perfectly crystallized and do not demonstrate any extended defects. Although at small magnification particles in the Mn_2O_3_wet3 sample look round, at high magnification they appear faceted (Figures 7b, d). High resolution [$01\bar{1}$] HAADF-STEM images show that the dominating straight facets are confined to the {111} crystal planes of the cubic bixbyite structure (Figures 7b, d). The assignment of the atomic columns to the contrast features in the HAADF-STEM image is provided in Figure S6 of the ESI. The round particle edges are formed by short segments of the {111} planes limited by steps of one or two atomic layers along another symmetry-related {111} plane. The surface of the particles is clean and does not show any amorphous matter or substantial atomic disorder. In comparison with Mn_2O_3_wet3, the Mn_2O_3_wet1 sample demonstrates longer and more perfect {111}-terminated surfaces (Figure 8f).

In order to make sure that an exposure to an alkaline environment (in the presence of oxygen) does not lead to either re-structuring or amorphization of the pristine surface, the Mn_2O_3_wet3 sample was examined with HAADF-STEM after 72h exposure to 1 M NAOH under ambient conditions. No visible changes were detected in the particle's shape and size and their surface structure (compare Figures 7a,b and Figures 7c,d).

5. Discussion

By studying a set of single and complex Mn oxides with RDE voltammetry, we have demonstrated that electrocatalytic activities of Mn oxides are grossly different even if they

contain Mn(III), which from the point of view of molecular orbital considerations is expected to satisfy the requirements of an optimum catalyst. It is also shown that the activity exhibits a remarkable correlation with the potential of the interfacial Mn(IV)/Mn(III) red-ox couple, the latter being directly related to the Gibbs energy difference for surface adsorbates O_{ad} and OH_{ad} ($E_1°=(\Delta G_O - \Delta G_{OH})/F$ *cf.* scheme presented in Figure 1). The surface-weighted catalytic activity in the electrochemical ORR increases exponentially with the potential of the interfacial Mn(IV)/Mn(III) red-ox couple. Overall activity gain by the 100 mV potential shift of the red-ox peak is ca. 40-fold at 0.9 V vs. RHE. Although the importance of red-ox transitions of a transition metal cation for the ORR/OER has been evoked in previous publications, the M(n+1)/M(n) potential has never been so clearly demonstrated to act as a descriptor of the ORR activity. This provides a simple means to screen catalytic materials for the ORR.

We rationalize the observed ORR activity *vs* Mn(IV)/Mn(III) potential dependence using a simple mean-field kinetic model considering that O_2 adsorption can only occur on Mn(III) centers, which are oxidized to Mn(IV) during the catalytic cycle, and have to be converted back to Mn(III) thus requiring a fast red-ox step. Note that at variance with Su *et al.* [27], our kinetic model considers the active site coverage effects. This is why our model proposes $E_1°=(\Delta G_O - \Delta G_{OH})/F$ as a the activity descriptor, while Su *et al.* [27] based on their DFT study, suggest ΔG_{OH} as a unique descriptor of the ORR electrocatalysis. That may explain why according to Su et al. [27] Mn_2O_3, MnO_2 and Mn_3O_4 are expected to have the same activity, which, however, is not supported by this work. Our model also predicts that besides the red-ox potential, the adsorbate-adsorbate interactions may also strongly affect the ORR activity, repulsive interactions in the adlayer favoring availability of Mn(III) sites, where the reaction occurs.

Between different Mn oxides explored in this work, Mn_2O_3 samples exhibit unprecedentedly high mass and specific activities in the ORR, which can hardly be matched by the values previously published in the literature (Table 2). Different specific surface areas, crystallite size, and density of the surface terraces for the Mn_2O_3 samples result in virtually

identical specific activity, measured currents increasing with the increase of the specific surface area. Such striking independence points towards a fundamental relation between the specific catalytic activity and the crystal structure of the material, which can be traced through the established kinetic ORR current –surface red-ox potential correlation. Heterogeneous catalysis and electrocatalysis are surface phenomena and correlation of the bulk structure with the surface reactivity is not straightforward. Admitting an obvious fact that the interfacial structure is different from that of the bulk, one cannot ignore, however, that the latter affects the surface structure. Citing recent perspective of Wachs and Routray, one may say that "…the function of the bulk mixed oxide phase is to serve as a unique support for the surface catalytic active sites…" [43]. From this point of view materials of various crystal structures could be treated as templates affecting their surface red-ox properties.

In all studied compounds Mn(III) cations are in octahedral coordination, with a pronounced Jahn-Teller distortion, but differ in the connectivity of the MnO_6 octahedra (Mn_3O_4 contains tetrahedrally coordinated Mn(II) cations as well). In the crystal structures of γ-MnOOH and α-Mn_2O_3 corner and edge sharing takes place with the shortest Mn-Mn distances of ~2.78 Å and 3.10 Å, respectively [44] [45]. In the perovskite structure octahedra are connected by corners only, with large (~3.85 Å) distance between the Mn(III) cations [46].

γ-MnOOH and β-MnO_2, which show the lowest ORR activity in the studied series of materials, have very similar rutile-like structure (Figure 2). Crystal structure of β-MnO_2 consists of nearly regular MnO_6 octahedra with Mn-O bond lengths spanning from 1.884 Å (equatorial) to 1.897 Å (axial) [47]. In the case of γ-MnOOH, MnO_6 octahedra are rather distorted due to the presence of Jahn-Teller Mn(III) cation, metal-oxygen bond distances spanning from 1.881-1.982 Å for Mn-O to 2.213 Å, 2.337 Å for Mn-OH [44]. We infer that it is the small perturbation of the crystal structure accompanying the Mn(IV)/Mn(III) red-ox process, which accounts for a small value of $\Delta G_O - \Delta G_{OH}$ and the correspondingly low E_f for γ-MnOOH and β-MnO_2.

Perovskite and spinel structures are known for their flexibility and can accommodate cations with different crystal chemistry and charges. Structural reorganization concomitant to the red-ox transition is relatively small resulting in an intermediate (between MnOOH and Mn_2O_3) value of red-ox potentials for these materials.

α-Mn_2O_3 (bixbyite, Figure 2a) crystallizes in the oxygen-deficient fluorite-related structure. Among M_2O_3 oxides with *d*-metal cations Mn_2O_3 is the only one having such a unique crystal structure. Oxygen anions are shared by four Mn(III) cations and are strongly bound. Stabilization of this structure requires presence of trivalent large cations like Sc, In, Rare Earth etc, or Jahn-Teller cations like Mn(III), hindering oxidation of the latter to a much smaller Mn(IV). Even though the Mn(IV)/Mn(III) redox transition under the ORR conditions is expected to be confined to the surface [48], where atoms have higher degree of freedom to adopt to the changes in the red-ox state, the bixbyite structure requires significant reorganization to allow the red-ox transformation to occur. This results in a higher Mn(IV)/Mn(III) potential, offering Mn(III) active sites for the O_2 adsorption at high potentials, and accelerates the rate of the ORR in the case of α-Mn_2O_3.

Thus, the observed differences in the catalytic activities between the investigated Mn oxides may be explained by different connectivity of MnO_6 octahedra in their crystal structures. The latter affects the flexibility of the crystal structure, and its capability to adapt to surface red-ox transitions, and thus determines the value of their surface red-ox potential. The highest activity of Mn_2O_3 compared to other single or complex oxides is likely to be related to the singularity of bixbyite structure, which fits larger Mn(III) rather than smaller Mn(IV) cations. To sum up, we attribute the exceptional total activity of Mn_2O_3 observed in this work to (i) its unique crystal structure, resulting in favorable properties of the interfacial Mn(IV)/Mn(III) red-ox couple; (ii) the integrity of the oxide structure studied in the range of the oxide stability; (iii) its high specific surface area (for Mn_2O_3_wet3), (iv) the optimized composition and the preparation procedure of the oxide/carbon electrode.

In the future, deeper understanding of the influence of the surface and bulk structure on the kinetics of different ORR steps requires application of *in situ* spectroscopies (such as Raman and Near-Ambient Pressure X-Ray Photoelectron Spectroscopy [49] [50]), combining mean-field kinetic modeling with quantum chemical approach to the description of the reaction layer, and estimation of rate constants for key elementary steps of oxygen electrocatalysis in the frames of modern charge transfer theory. The present study calls for further investigations in order to define the limits of the discovered exponential dependence of the ORR activity on the surface red-ox potential and its applicability to other catalytic systems with different structures and chemical compositions.

6. Conclusions

A set of binary and complex Mn oxides was investigated as catalysts of the electrochemical oxygen reduction reaction using rotating disc electrode method. It was demonstrated that their electrocatalytic activity correlates with the potential of the surface Mn(IV)/Mn(III) red-ox couple, suggesting the latter as a new descriptor for the ORR electrocatalysis. The observed dependence is rationalized using a mean-field kinetic model, which considers the surface site availability and adsorbate-adsorbate interactions. Among studied Mn oxides, Mn_2O_3 demonstrates an unprecedented catalytic activity, which is attributed to (i) its unique crystal structure; (ii) the integrity of the oxide structure studied in the range of the oxide stability; (iii) its high specific surface area, (iv) the optimized composition and the preparation procedure of the oxide/carbon electrode.

Acknowledgements:

The authors thank P. Simonov of the Boreskov Institute of Catalysis (Novosibirsk, Russia) for supplying Sibunit Carbon, and Tokuyama Company for supplying alkaline ionomer. Financial support from CNRS (France) within PICS project, Russian Foundation for Basic Research (project number 13-03-91054), and French Ministry of Foreign Affairs and International Development for Eiffel scholarship to A.R. is gratefully appreciated.

References

[1] *Z. Zhang, J. Liu, J. Gu, J., L. Su, L. Cheng, An overview of metal oxide materials as electrocatalysts and supports for polymer electrolyte fuel cells,* Energy Environ. Sci. 7 (2014) 2535.

[2] *C. Fangyi, C. Jun, Metal-air batteries: from oxygen reduction electrochemistry to cathode catalysts,* Chem. Soc. Rev. 41 (2012) 2172.

[3] *J.W.D. Ng, Y. Gorlin, T. Hatsukade, T.F.A. Jaramillo, A precious-metal-free regenerative fuel cell for storing renewable electricity,* Adv. Energy Mater. 3 (2013) 1545.

[4] *K. A. Stoerzinger, M. Risch, B. Han, and Y. Shao-Horn, Recent Insights into Manganese Oxides in Catalyzing Oxygen Reduction Kinetics,* ACS Catal. 5 (2015) 6021–6031.

[5] *Steven F. Bender, John W. Cretzmeyer, and Terrence F. Reise, ZINC/AIR BATTERIES—BUTTON CONFIGURATION, In: Handbook of Batteries, David Linden and Thomas B. Reddy Eds, 3rd Edition, 2002, N-Y, McGraw-Hill, Chapter 13, p.13.1-13.21.*

[6] *H.N. Cong, P. Chartier, J. Brenet, Reduction electrocatalytique de l'oxygene sur electrodes solides d'oxydes mixtes contenant des ions manganese. II. Role du couple Mn 3+ - Mn 4+ en sites octaédriques,* J. Appl. Electrochem. 7 (1977) 395.

[7] *J.P. Brenet, Electrochemical behaviour of metallic oxides,* J. Power Sources. 4 (1979) 183.

[8] *L. Mao, D. Zhang, T. Sotomura, K. Nakatsu, N. Koshiba, T. Ohsaka , Mechanistic study of the reduction of oxygen in air electrode with manganese oxides as electrocatalysts,* Electrochim. Acta 48 (2003) 1015.

[9] *I. Roche, E. Chainet, M. Chatenet, J. Vondrak, Carbon-supported manganese oxide nanoparticles as electrocatalysts for the oxygen reduction reaction (ORR) in alkaline medium: physical characterizations and ORR mechanism,* J. Phys. Chem. C 111 (2007) 1434.

[10] *F.H.B. Lima, M.L. Calegaro, E.A. Ticianelli, Electrocatalytic activity of manganese oxides prepared by thermal decomposition for oxygen reduction,* Electrochim. Acta 52 (2007) 3732.

[11] *Q.W. Tang, L.H. Jiang, J. Liu, S.L. Wang, G.Q. Sun, Effect of surface manganese valence of manganese oxides on the activity of the oxygen reduction reaction in alkaline media,* ACS Catal. 4 (2014) 457.

[12] *A.C. Garcia, A.D. Herrera, E.A. Ticianelli, M. Chatenet, C. Poinsignon, Evaluation of several carbon-supported nanostructured Ni-doped manganese oxide materials for the electrochemical reduction of oxygen,* J. Electrochem. Soc. 158 (2001) B290.

[13] *F. Cheng, Y. Su, J. Liang, Z. Tao, J. Chen, MnO2-based nanostructures as catalysts for electrochemical oxygen,* Chem. Mater. 22 (2010) 898.

[14] *W.G. Hardin, J.T. Mefford, D.A. Slanac, B.B. Patel, X. Wang, S. Dai, X. Zhao, R.S. Ruoff, K.P Johnston, K.J. Stevenson, Tuning the electrocatalytic activity of perovskites through active site variation and support interactions,* Chem. Mater. 26 (2014) 3368.

[15] *E. Fabbri, R. Mohamed, P. Levecque, O. Conrad, R. Koetz, T.J. Schmidt, Composite electrode boosts the activity of Ba0.5Sr0.5Co0.8Fe0.2O3-delta perovskite and carbon toward oxygen reduction in alkaline media,* ACS Catal. 4 (2014) 1061.

[16] *S. Malkhandi, P. Trinh, A.K. Manohar, K.C. Jayachandrababu, A. Kindler, G.K.S. Prakash, S.R. Narayanan, Electrocatalytic activity of transition metal oxide-carbon composites for oxygen reduction in alkaline batteries and fuel cells,* J. Electrochem. Soc. 160 (2013) F943.

[17] *T. Poux, F.S. Napolskiy, T. Dintzer, G. Kéranguéven, S. Ya. Istomin, G.A. Tsirlina, E.V. Antipov, E.R. Savinova, Dual role of carbon in the catalytic layers of perovskite/carbon*

composites for the electrocatalytic oxygen reduction reaction, Catal. Today. 189 (2012) 83.

[18] *K. Kinoshita, Carbon – Electrochemical and Physicochemical Properties,* Wiley, New York (USA), 1988.

[19] *E. Fabbri, A. Habereder, K. Waltar, R. Kötz, T.J. chmidt, Developments and perspectives of oxide-based catalysts for the oxygen evolution reaction,* Catal. Sci. Technol. 4 (2014) 3800.

[20] *P. Ruetschi, P. Delahay, Influence of electrode material on oxygen overvoltage - a theoretical analysis,* J. Chem. Phys. 23 (1955) 556.

[21] *J.O'M. Bockris, T. Otagawa, Mechanism of oxygen evolution on perovskites,* J. Phys. Chem. 87 (1983) 2960.

[22] *C.C. Tseung, S. Jasem, Oxygen evolution on semiconducting oxides,* Electrochim. Acta. 22 (1977) 31.

[23] *S. Trasatti, Electrocatalysis by oxides - attempt at a unifying approach,* Electroanal. Chem. 111 (1980) 125.

[24] *J.B. Goodenough, B.L. Cushing, Oxide-based ORR catalysts,* in W. Vielstich, H. A. Gasteiger, H. Yokokawa (Eds.), Handbook of Fuel Cells—Fundamentals, Technology and Applications, Vol. 2, Wiley, 2003, p. 520.

[25] *J. Suntivich, H.A. Gasteiger, N. Yabuuchi, H. Nakanishi, J.B. Goodenough, Y. Shao-Horn, Design principles for oxygen-reduction activity on perovskite oxide catalysts for fuel cells and metal-air batteries,* Nat. Chem. 3 (2011) 546.

[26] *W.T. Hong, M. Risch, K.A. Stoerzinger, A. Grimaud, J. Suntivich, Y. Shao-Horn, Toward the rational design of non-precious transition metal oxides for oxygen electrocatalysis,* Energy Environ. Sci. 8 (2015) 1404.

[27] *H.Y. Su, Y. Gorlin, I.C. Man, F. Calle-Vallejo, J.K. Nørskov, T.F. Jaramillo, J. Rossmeisl,* Identifying active surface phases for metal oxide electrocatalysts: a study of manganese oxide bi-functional catalysts for oxygen reduction and water oxidation catalysis, Phys. Chem. Chem. Phys. 1 (2012) 14010.

[28] *T. Poux, A. Bonnefont, A. Ryabova, G. Kéranguéven, G. A. Tsirlina, E. R. Savinova, Electrocatalysis of hydrogen peroxide reactions on perovskite oxides: experiment versus kinetic modeling,* Phys. Chem. Chem. Phys. 16 (2014) 13595.

[29] *T. Poux, A. Bonnefont, G. Kéranguéven, G.A. Tsirlina, E.R. Savinova, Electrocatalytic oxygen reduction reaction on perovskite oxides: series versus direct pathway,* Chem. Phys. Chem. 15 (2014) 2108.

[30] *Y. Gorlin, B. Lassalle-Kaiser, J.D. Benck, S. Gul, S.M. Webb, V.K. Yachandra, J. Yano, T.F. Jaramillo,* In situ X-ray absorption spectroscopy investigation of a bifunctional manganese oxide catalyst with high activity for electrochemical water oxidation and oxygen reduction, J. Am. Chem. Soc. 135 (2013) 8525.

[31] *J. McBreen, The electrochemistry of β-MnO2 and γ-MnO2 in alkaline electrolyte,* Electrochim. Acta 20 (1975) 221.

[32] *V.M.B. Crisostomo, J.K. Ngala, S. Alia, A. Dobley, C. Morein, C.-H. Chen, X. Shen, S.L. Suib, New synthetic route, characterization, and electrocatalytic activity of nanosized manganite,* Chem. Mater. 19 (2007) 1832.

[33] *S.H. Ju, D.Y. Kim, H.Y. Koo, S.K. Hong, E.B. Jo, Y.C. Kang, The characteristics of nano-sized manganese oxide particles prepared by spray pyrolysis,* J. Alloys and Comp. 425 (2006) 411.

[34] *X. Cao, N. Wang, L. Wang, C. Mo, Y. Xu, X. Cai, L. Guo, A novel non-enzymatic hydrogen peroxide biosensor based on ultralong manganite MnOOH nanowires,* Sensors and Actuators B 147 (2010) 730.

[35] *A. Douy, Polyacrylamide gel: an efficient tool for easy synthesis of multicomponent oxide*

precursors of ceramics and glasses, Int. J. Inorg. Mater. 3 (2001) 699.

[36] *P. Scardi, M. Leoni, Whole powder pattern modelling,* Acta Cryst. A 58 (2002) 190.

[37] *M. Leoni, T. Confente, P. Scardi, PM2K: a flexible program implementing Whole Powder Pattern Modelling,* Z. Kristallogr. 23 (2006) 249.

[38] *Y.I. Yermakov, V.F. Surovikin, G.V. Plaksin, V.A. Semikolenov, V.A. Likholobov, L.V. Chuvilin, S.V. Bogdanov, New carbon material as support for catalysts,* Reaction Kinetics and Catalysis Lett. 33 (1987) 435.

[39] *V. Rao, P.A. Simonov, E.R. Savinova, G.V. Plaksin, S.V. Cherepanova, G.N. Kryukova, U. Stimming, The influence of carbon support porosity on the activity of PtRu/Sibunit anode catalysts for methanol oxidation,* J. Power Sources 145 (2005) 178.

[40] *B. Messaoudi, S. Joiret, M. Keddam, H. Takenouti,Anodic behavior of manganese in alkaline medium,* Electrochim. Acta 46 (2001) 2487.

[41] *P. Nkeng, S. Marlier, J.F. Koenig, P. Chartier, G. Poillerat, J.L. Gautier, Real surface determination of Co3O4 by Zn2+ adsorption. A comparison between X-ray diffraction, cyclic voltammetry and adsorption methods,* Electrochim. Acta 43 (1998) 893.

[42] *J. Masa, K. Ozoemena, W. Schuhmann, J.H. Zagal, Oxygen reduction reaction using N4-metallomacrocyclic catalysts: fundamentals on rational catalyst design,* J. Porphyrins Phthalocyanines 16 (2012) 761.

[43] *I.E. Wachs, K. Routray, Catalysis science of bulk mixed oxides,* ACS Catal. 2 (2012) 1235.

[44] *T. Kohler, T. Armbruster, E. Libowitzky, Hydrogen bonding and Jahn-Teller distortion in groutite, alpha-MnOOH, and manganite, gamma-MnOOH, and their relations to the manganese dioxides ramsdellite and pyrolusite,* J. Solid State Chem. 133 (1997) 486.

[45] *S. Geller, Structures of alfa-Mn2O3, (Mn0.983Fe0.017)2O3 and (Mn0.37Fe0.63)2O3 and relation to magnetic ordering,* Acta Crystallographica B 27 (1971) 821.

[46] *J.B.A.A. Elemans, B. van Laar, K.R. van der Veen, B.O. Loopstra, Crystallographic and magnetic structures of La1-xBaxMn1-xMexO3 (Me=Mn or Ti),* J. Solid State Chem. 3 (1971) 238.

[47] *A.A. Bolzan, C. Fong, B.J. Kennedy, C.J. Howard, Powder neutron diffraction of pyrolusite, betta-MnO2,* Australian J. Chem. 46 (1993) 939.

[48] *Y. Gorlin, T.F. Jaramillo, Investigation of surface oxidation processes on manganese oxide electrocatalysts using electrochemical methods and ex situ X-ray photoelectron spectroscopy,* J. Electrochem. Soc. 159 (2012) H782.

[49] *Y.-T. Law, S. Zafeiratos, S. G. Neophytides, A. Orfanidi, D. Costa, T. Dintzer, R. Arrigo, A. Knop-Gericke, R. Schlögl and E. R. Savinova,* In situ investigation of dissociation and migration phenomena at the Pt/electrolyte interface of an electrochemical cell, Chem. Sci., 2015, 6, 5635-5642.

[50] *V. Papaefthimiou, M. Diebold, C. Ulhaq-Bouillet, W. Hui Doh, R. Blume, S. Zafeiratos, and E. R. Savinova,* Potential-Induced Segregation Phenomena in Bimetallic PtAu Nanoparticles: An In Situ Near-Ambien-Pressure Photoelectron Spectroscopy Study; ChemElectroChem, 2 (2015) 1519 – 1526.

[51] *Y. Gorlin, T.F. Garamillo, A bifunctional nonprecious metal catalyst for oxygen reduction and water oxidation,* J. Am. Chem. Soc. 132 (2010) 13612.

[52] *J. Suntivich, E.E. Perry, H.A. Gasteiger, Y. Shao-Horn, The influence of the cation on the oxygen reduction and evolution activities of oxide surfaces in alkaline electrolyte,* Electrocatal. 4 (2013) 49.

Figure Captions

Figure 1. Proposed oxygen reduction mechanism. Step 1 is O_{ad}/OH_{ad} conversion accompanied by Mn(IV)/Mn(III) red-ox transition (Mn(IV)=O/Mn(III)-OH). Step 2 is electrochemical O_2 adsorption, which proceeds via displacement of adsorbed OH species accompanied by an electron transfer, and can only occur on Mn(III) sites (green). Step 3 is coupled electron and proton (from water molecule) transfer. Step 4 is adsorption/ desorption of hydrogen peroxide, the latter dissociating into HO_2^- in alkaline medium. Step 5 is a chemical step resulting in formation of two Mn(IV) sites (red). For further details see text and Electronic Supplementary Information (ESI).

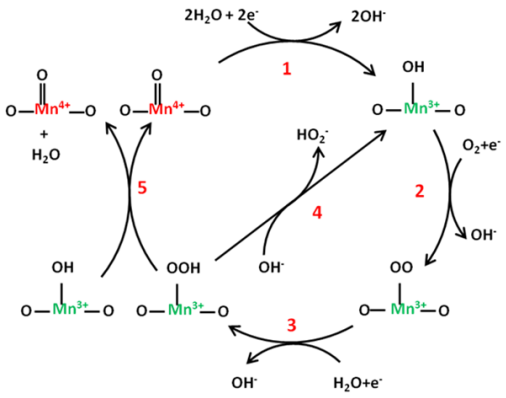

Figure 2. Crystal structures of Mn oxides studied in this work: (a) α-Mn_2O_3 (bixbyite), (b) α-MnOOH (manganite), (c) β-MnO_2 (pyrolusite) (d) $LaMnO_3$ (perovskite-type) and (e) Mn_3O_4 (spinel).

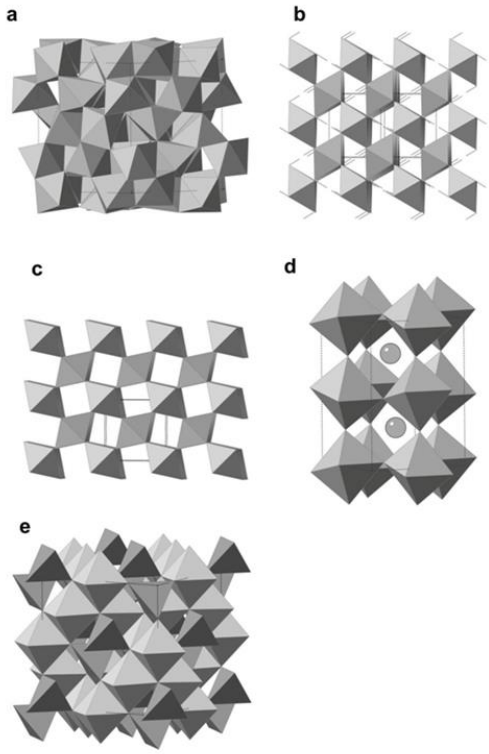

Figure 3. Representative SEM images of the prepared Mn oxides: (a) MnOOH; (b) MnO_2; (c) Mn_3O_4, (d) Mn_2O_3_wet1; (e) Mn_2O_3_wet3; (f) Mn_2O_3 milled; (g) $LaMnO_3$; (h) $PrMnO_3$; (i) $La_{0.8}Ca_{0.2}MnO_3$.

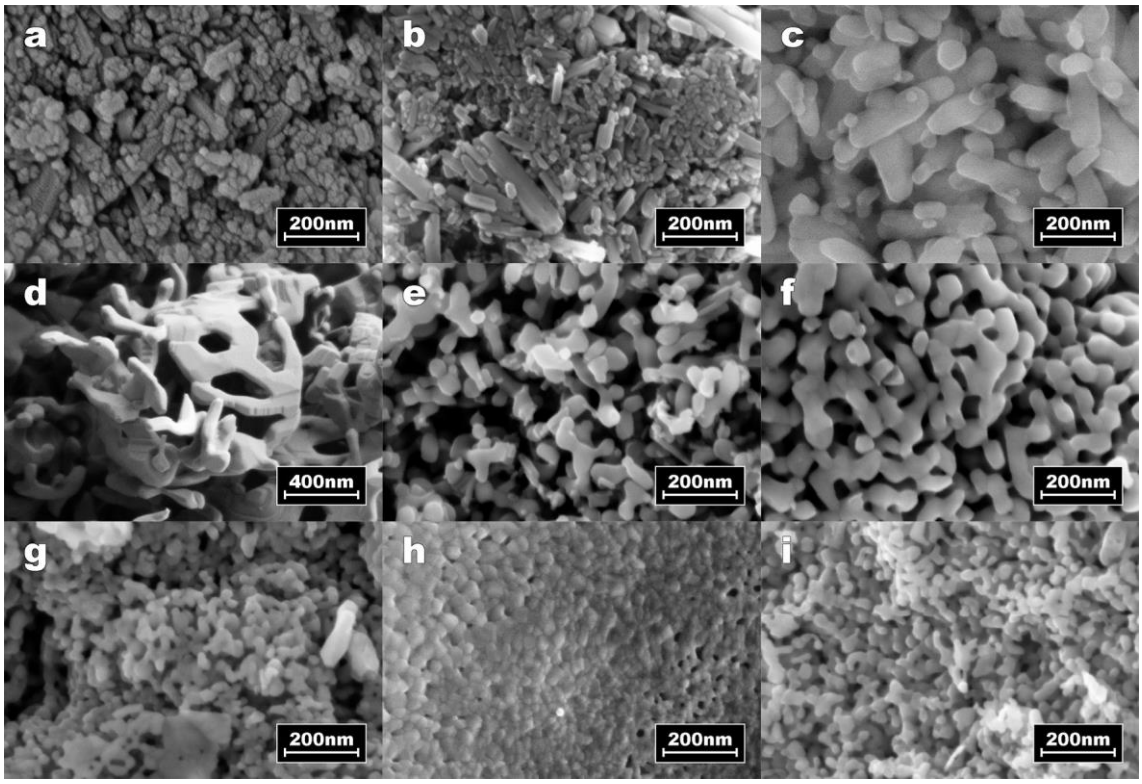

Figure 4. Experimental CVs with decreasing cathodic potential limit for GC-supported thin films of oxide/carbon composites in N_2-purged 1 M NaOH at 10 mV s^{-1} for $LaMnO_3$ (a), Mn_2O_3_milled (b), MnO_2 (c), and MnOOH (d). Currents are normalized to the geometric area of the electrode, and corrected to the background currents measured on Sibunit carbon under the same conditions.

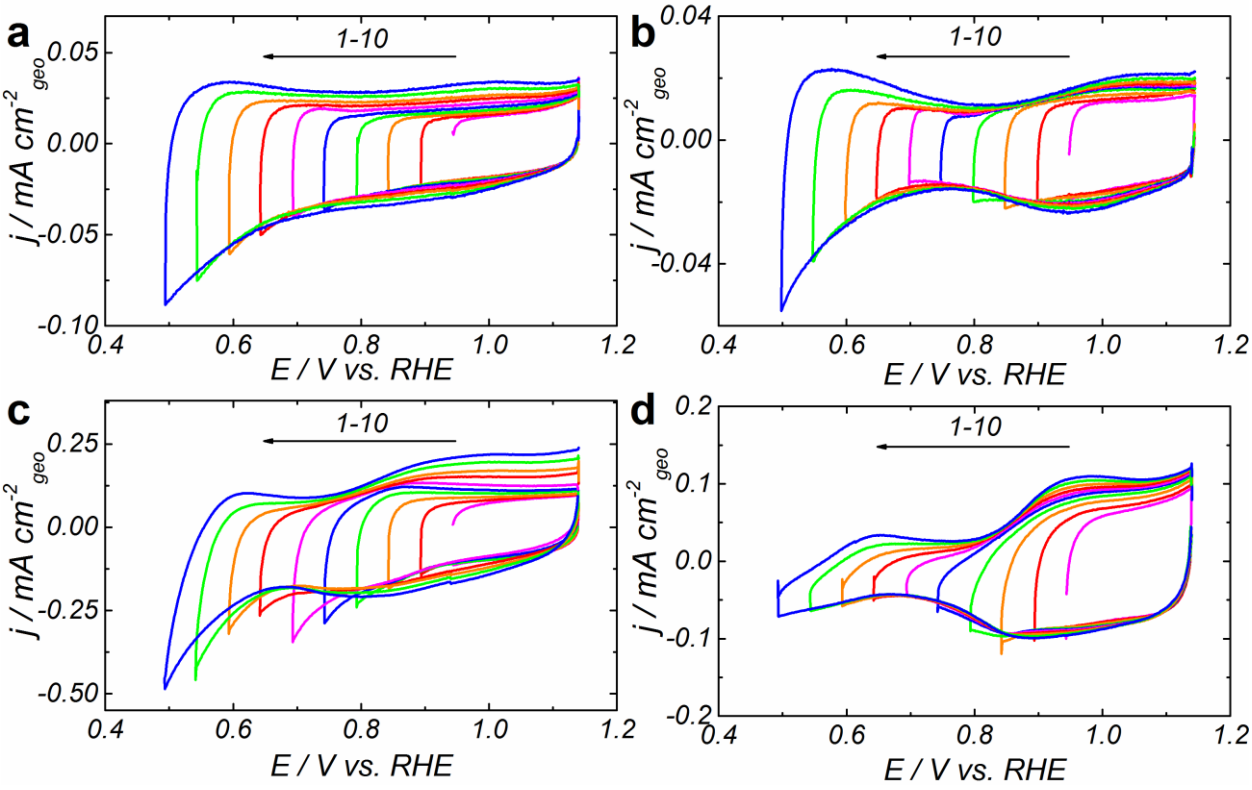

Figure 5. CVs in N_2-saturated 1M NaOH (a), and RDE voltammograms in O_2-saturated 1M NaOH at 900 rpm (b) for selected samples, the corresponding Tafel plots (c), and kinetic ORR currents at 0.9 V vs. RHE *vs.* E_f (d). For sample numbers refer to Table 1. Color and symbol codes: Mn_2O_3_milled (stars, red), Mn_2O_3_wet1 (diamonds, red), Mn_2O_3_wet3 (circles, red), $LaMnO_3$ (stars, cyan), $PrMnO_3$ (diamonds, cyan), $La_{0.8}Ca_{0.2}MnO_3$ (circles, cyan), MnO_2 (circles, blue), MnOOH (circles, green), Mn_3O_4 (circles, wine). Considering its cathodic degradation, RDE curves and kinetic currents for MnO_2 are shown for two cathodic limits (0.75 V, non-degraded, solid line, labelled as 7) and (0.65 V, degraded, dashed line, labelled as 7'). Error bars represent standard deviation from at least two independent repeated measurements.

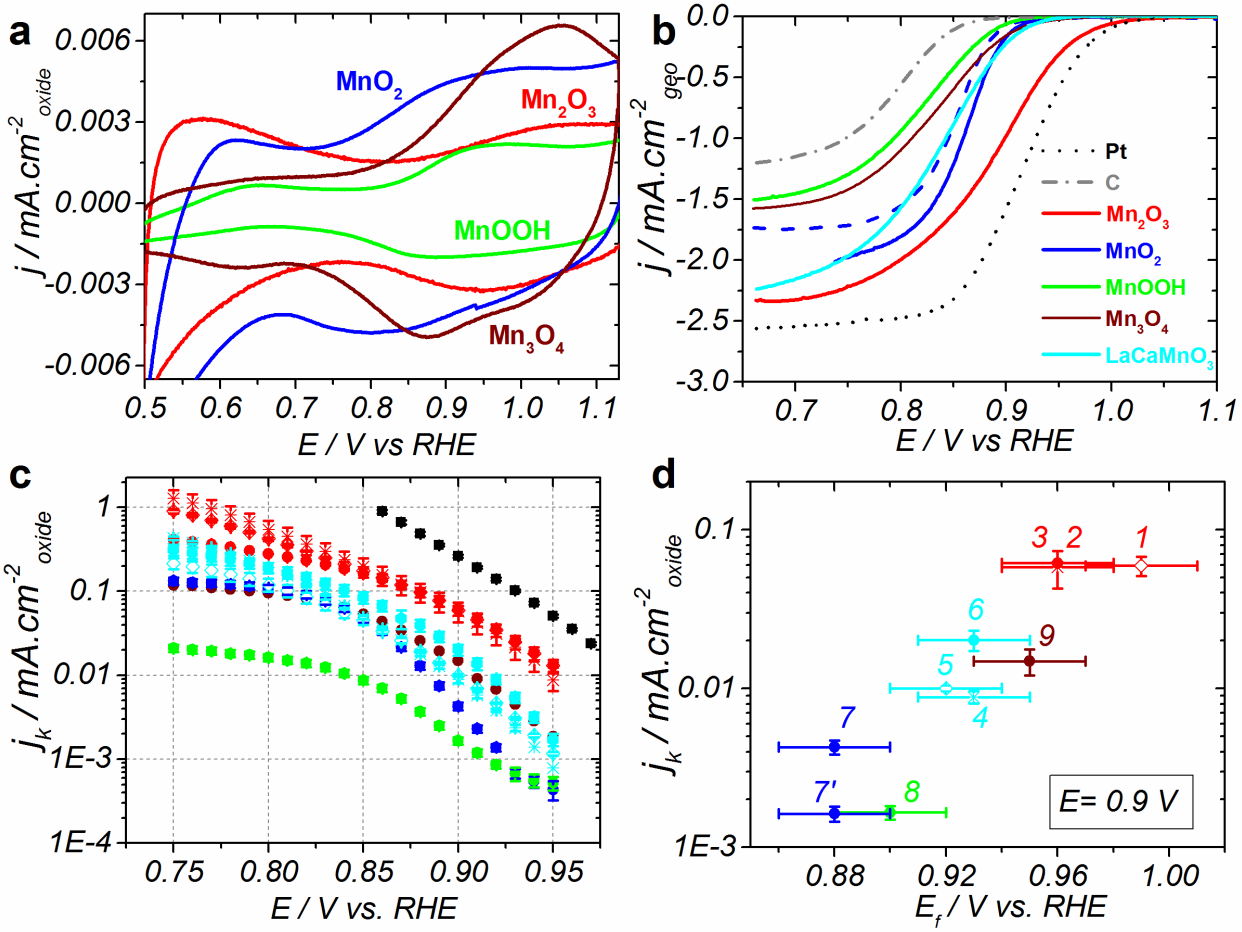

Figure 6. Koutecky–Levich plots at 0.65 V vs. RHE constructed from RDE data acquired at various rotating rates for different Mn oxides, Pt/C and carbon (Sibunit) in O_2-saturated 1M NaOH. Error bars represent standard deviation from at least two independent repeated measurements. Dashed lines show slopes calculated for a 4e (grey) and 2e ORR (khaki).

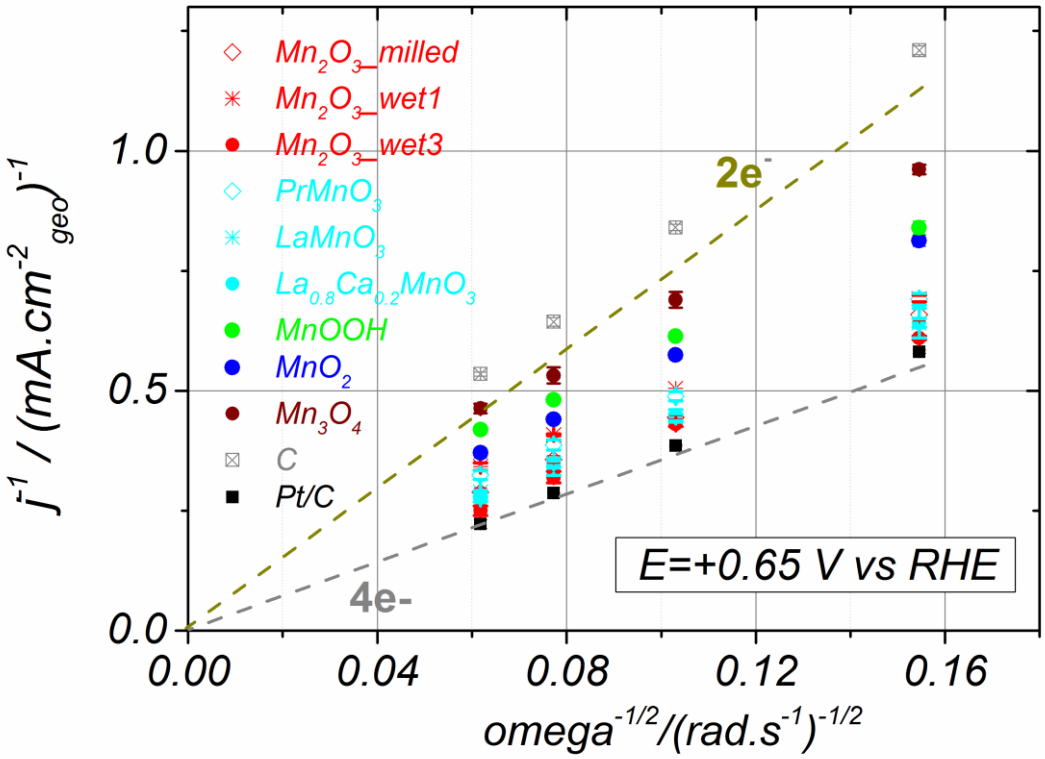

Figure 7. Simulated CVs (a, b), O_{ad} adsorption isotherms (c), RDE ORR curves (d), Tafel plots (e), and kinetic ORR currents *vs*. the E_f potential for the Mn(IV)/Mn(III) redox transition (f). Color codes for panels (a)-(e): E_1° =0.85 V, γ = 0 (magenta); E_1° =0.85 V, γ = 6 (blue); E_1° =0.85 V, γ = 10 (green); E_1° =0.95 V, γ = 0 (black); E_1° =0.95 V, γ = 6 (red). For further details see text.

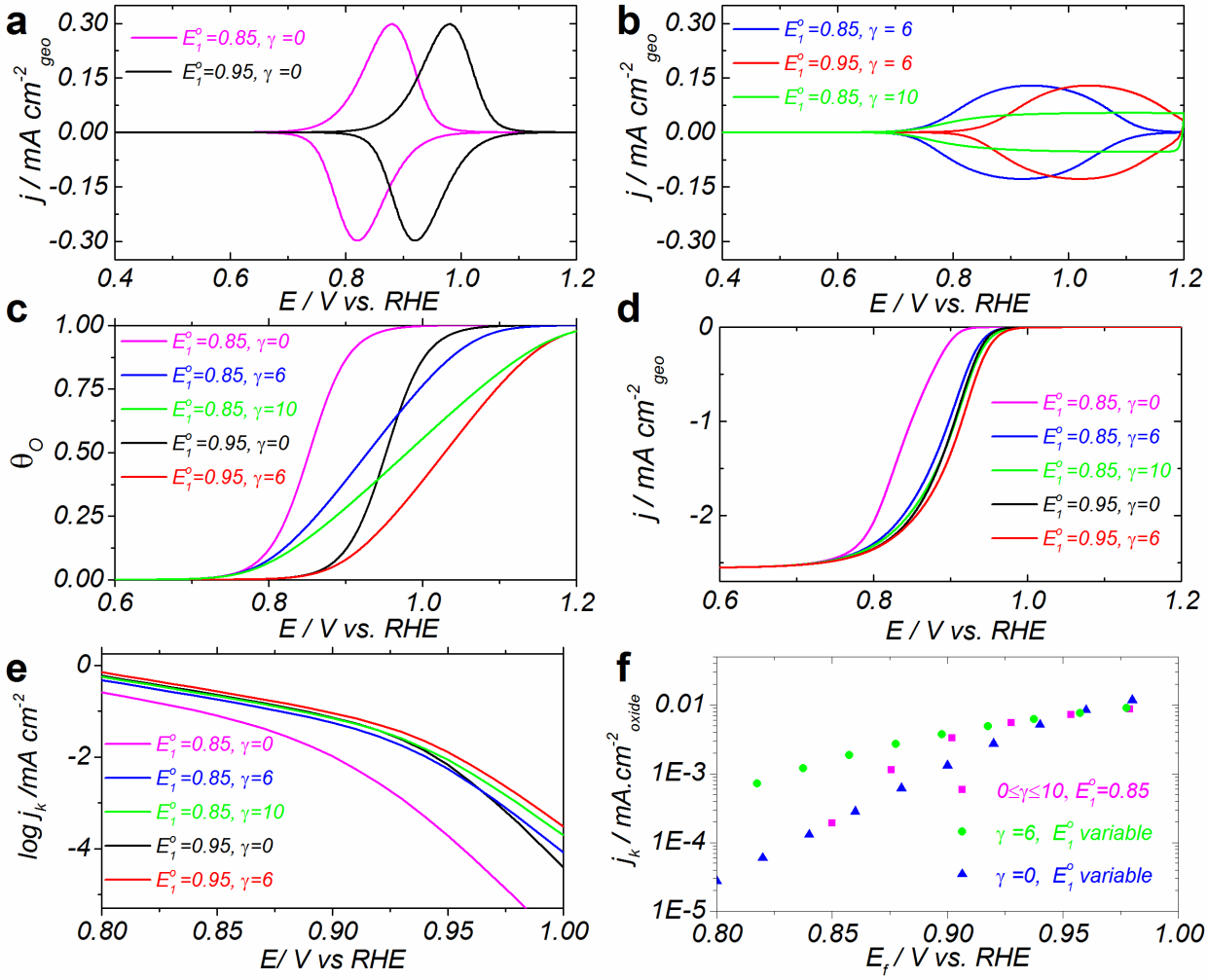

Figure 8. HAADF-STEM images of the interconnected Mn_2O_3 nanoparticles in the pristine Mn_2O_3_wet3 sample (a), Mn_2O_3_wet3 sample kept in alkaline solution at room temperature for 72 hours (c) and Mn_2O_3_wet1 sample (e). High resolution $[01\bar{1}]$ HAADF-STEM images showing terraced surface of the particles with dominating {111} crystal planes (b, d, f: the same sequence of samples).

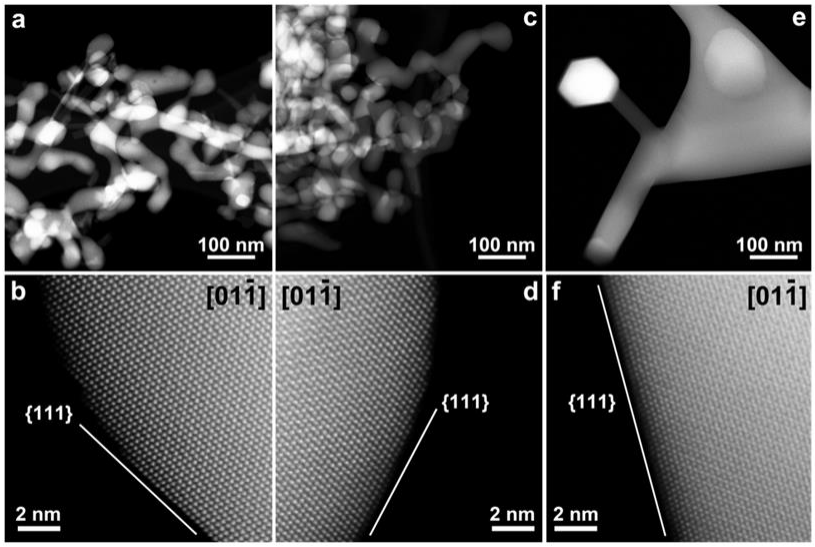

Table 1. Structural, morphological and electrochemical characteristics of Mn oxides

No	Sample notation	Main phase* (structure type)	BET area, m^2g^{-1}	E_f,† V vs RHE	n_{eff}††
1	Mn_2O_3_milled	α-Mn_2O_3 (bixbyite)	8	0.99	3.8
2	Mn_2O_3_wet_1	α-Mn_2O_3 (bixbyite)	3	0.96	3.9
3	Mn_2O_3_wet_3	α-Mn_2O_3 (bixbyite)	27	0.96	3.9
4	$LaMnO_3$	$LaMnO_3$ (perovskite)	14	0.93	3.8
5	$PrMnO_3$	$PrMnO_3$ (perovskite)	18	0.92	3.7
6	$La_{0.8}Ca_{0.2}MnO_3$	$La_{0.8}Ca_{0.2}MnO_3$ (perovskite)	20	0.93	3.7
7	MnO_2	β-MnO_2 (pyrolusite)	48	0.88	3.0
8	MnOOH	α-MnOOH (manganite)	55	0.90	3.1
9	Mn_3O_4	Mn_3O_4 (hausmannite)	13	0.95	2.7
10	Pt/C		-	-	3.9
11	Sibunit carbon		66	-	2.0

* Determined from XRPD patterns presented in Figure S3.

† Formal potential for Mn(IV)/Mn(III) interfacial red-ox transition E_f determined with the accuracy of ±0.02 V. Refer to Figure S4 for the explanation of how E_f is calculated from the experimental CVs.

†† Effective number of electrons transferred in the ORR (n_{eff}) and determined from the slope of Koutecky-Levich plots (see Figure 6).

Table 2. Comparison of ORR activities found in this work with some representative literature data

Sample	Specific surface area of oxide, m^2g^{-1}	Oxide /carbon loading, µg cm^{-2}	Electrolyte*/T °C	Potential limits vs.RHE	Half-wave potential, vs.RHE	Specific activity at 0.9 V vs. RHE, µA cm^{-2}	Mass Activity at 0.9 V vs. RHE, A g^{-1}	Ref
Mn_2O_3_wet_3	27	91/91	1M NaOH/ 25	0.65 – 1.15	0.89	62	17	This work
Mn_2O_3	NA	1300/0	0.1 M KOH/ 25	-0.3 – 0.9	0.66	NA	NA	[8]
20% Mn_2O_3/Vulcan XC-72	NA	40/160	1 M KOH/ 25	0.05 – 1.5	0.75	NA	4	[10]**
MnOOH	55	91/91	1M NaOH/ 25	0.65 – 1.15	0.82	1.7	0.9	This work
$LaMnO_3$	14	91/91	1M NaOH/ 25	0.65 – 1.15	0.82	9	1.3	This work
$LaMnO_{3+\delta}$	0.5	250/50	0.1 M KOH	NA	NA	60	0.3	[25]
$La_{0.5}Ca_{0.5}MnO_3$	2.1	250/50	0.1 M KOH	NA	NA	10	0.2	[25]
Mn_3O_4	13	91/91	1M NaOH/ 25	0.65 – 1.15	0.83	15	2	This work
20% Mn_3O_4/Vulcan XC-72	NA	40/160	1 M KOH/ 25	0.05 – 1.5	0.80	NA	5	[10]**
β-MnO_2	48	91/91	1M NaOH/ 25	0.75 – 1.15	0.86	4	2	This work
20% β-MnO_2/Vulcan XC-72	NA	40/160	1 M KOH/ 25	0.05 – 1.5	0.82	NA	14	[10]**
20%MnOx/ C (Chezacarb SH)	280-350†	160/640	1 M KOH/ 25	0.31 – 1.01	NA	0.2-0.3††	0.75††	[9]
Ni-MnO*x*/C (Chezacarb SH)	200-270†	160/640	1 M KOH/ 25	0.31 – 1.01	0.83	0.9 – 1.3	2.6	[9]
MnO_x electrodeposited on GC	NA‡	NA	0.1 M KOH/ 23	0.05 – 1.8	0.73	NA	NA	[51]

* Note that Suntivich et al. [52] found significant effect of cations on the ORR at Pt, the activity increasing by ca. a factor of 2 from NaOH to KOH
** Potentials in the reference are given in Hg/HgO scale and recalculated into RHE scale via addition of + 0.93 V
† Recalculated from the data presented in the article as mass activity divided by specific activity
†† Recalculated from the data presented in the article considering the values of specific and mass activity at 0 V vs NHE and the value of the Tafel slope
‡ Oxide surface area estimated from cyclic voltammetry as 2.8 cm^2 (to be compared to ca. 24 cm^2 for Mn_2O_3_wet_3 in this work)